Proceedings of the ASME 2018 International Design Engineering Technical Conferences and Computers and Information in Engineering Conference IDETC/CIE 2018 August 26-29, 2018, Quebec City, Quebec, Canada

DETC2018-85871

A HYBRID COMPUTATIONAL AND ANALYTICAL MODEL OF INLINE DRIP EMITTERS

Jaya Narain*
Global Engineering and Research Laboratory
Department of Mechanical Engineering
Massachusetts Institute of Technology
Cambridge, MA
Email: jnarain@mit.edu

Amos G. Winter, V
Global Engineering and Research Laboratory
Department of Mechanical Engineering
Massachusetts Institute of Technology
Cambridge, MA
Email: awinter@mit.edu

ABSTRACT

This paper details a hybrid computational and analytical model to predict the performance of inline pressure-compensating (PC) drip irrigation emitters. The term inline refers to flow control devices mounted within the irrigation tubing. Pressure-compensating emitters deliver a relatively constant flow rate over a range applied pressure to accurately meter water to crops. Flow rate is controlled within the emitter by directing the water through a tortuous path (which imposes a fixed resistance), and then through a variable resistor composed of a flexible membrane that deflects under changes in pressure, restricting the flow path. An experimentally validated computational fluid dynamics (CFD) model was used to predict flow behavior through tortuous paths, and a pressure resistance parameter was derived to represent the pressure drop with a single variable. The bending and shearing mechanics of the membrane were modeled analytically and refined for accuracy by deriving a correction factor using finite element analysis. A least-squares matrix formulation that calculates the force applied by a line load of any shape, along which there is a prescribed deflection applied on a rectangular membrane, was derived and was found to be accurate to within one percent. The applicability of the assumption of locally fully developed flow through the pressure compensating chamber in a drip emitter was analyzed.

The combined hybrid computational-analytical model reduces the computational time of modeling drip emitter performance from days to less than 30 minutes, dramatically lowering the time required to iterate and select optimal designs. The model was validated using three commercially available drip emitters, rated at 1.1, 2, and 3.8 L/hr. For each, the model predicted the flow rate with an error of twenty percent or less, as compared to the emitter performance published by the manufacturer.

NOMENCLATURE

- a Membrane length, [m]
- b Membrane width, [m]
- D Flexural modulus of membrane, [Pa*m^3]
- D_h Hydraulic diameter, [m]
- E Young's modulus of membrane, [Pa]
- f Friction factor
- F_{lands} Magnitude of concentrated load, [N]
- G Shear modulus of membrane, [Pa]
- h Membrane thickness, [m]
- h_p Characteristic flow passage height, [m]
- H_A Membrane hardness, [degrees]
- h_{land} Distance between the surface on which the membrane rests and the top of the lands, [m]
- l_{ri} Inner land radius, [m]
- K_1 Flow resistance parameter through the tortuous path, relating P1 and P2
- K_{fric} Frictional losses through duct

*Address all correspondence related to ASME style format and figures to this author.

$K_{minorloss}$ Minor loss coefficient
K_{mt} Total flow resistance underneath the membrane
L Characteristic flow passage length, [m]
m y-coordinate of concentrated load, [m]
n x-coordinate of concentrated load, [m]
P_1 Pressure above membrane; input pressure from pipe, [Pa]
P_2 Pressure under membrane; pressure at the end of the tortuous path, [Pa]
P_a Atmospheric pressure, [Pa]
P_L Pressure at which membrane contacts the lands, [Pa]
Re_{D_h} Reynolds' number of flow with respect to hydraulic diameter, [-]
$S_p(y)$ Ratio of the deformation at a coordinate along the channel to the maximum deflection in the channel, [m]
q Loading applied during tension test of silicone rubber, [Pa]
U Characteristic flow passage velocity parallel to passage length, [m]
u Width of patch load, [m]
V Characteristic flow passage velocity perpendicular to passage length, [m]
v Length of patch load, [m]
v_{ave} Average flow velocity in duct, [m]
w_{bend} Total deflection of membrane before touching the lands, [m]
$w_{ch}(x)$ Deformation profile of membrane across width of channel, [m]
$w_{ch,max}$ Maximum deformation of membrane into channel, [m]
w_{conc} Deflection of membrane due to a concentrated load, [m]
w_{max} Maximum deflection measured during tension test with silicone rubber, [m]
$w_{normalized}(x)$ Normalized deflection profile for a clamped thick beam, [-]
$w_{uniform}$ Deflection of membrane due to uniform load, [m]
ε Absolute roughness of emitter material, [-]
η Vertical distance to center of patch load, [m]
ν Poisson's ratio of membrane
ρ Density of water, [kg/m^3]
τ Characteristic time describing the flow, [s]
ξ Horizontal distance to center of patch load, [m]

1 Introduction

This paper presents a hybrid computational and analytical model of inline drip emitters that predicts the flow rate of an inline emitter as a function of pressure, given an input geometry. Drip irrigation is a method of irrigation that delivers a steady, controlled flow of water directly to the roots of a plant. The emitters in the drip system regulate the water flow rate, ensuring that the crops throughout a field get approximately the same amount of water. This method of irrigation reduces water consumption

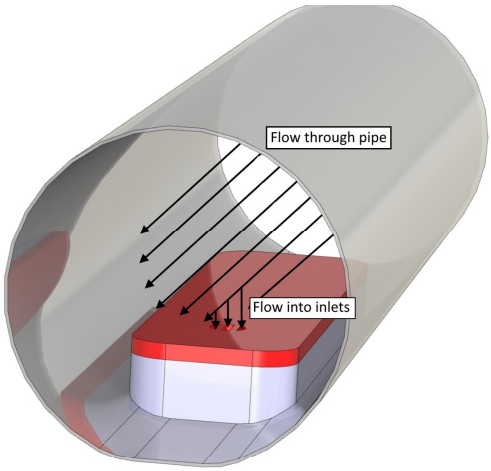

Figure 1. Inline emitters are embedded in pipes at the manufacturing stage. Water moves from the pipe into the emitter inlet

by preventing drainage and evaporation and can provide significant yield improvements over conventional methods of irrigation. A study conducted in India showed water savings between 20-40 percent and increases in yield between 20-50 percent with drip irrigation compared to furrow (flood) irrigation, depending on the crop grown [1]. Drip irrigation can enable farmers to grow crops under conditions where they could not otherwise do so (e.g. with strict water constraints or in dry seasons), allow farmers to grow a wider array of crops, and save on labor and fertilizer costs [2]. Reducing the activation pressure of drip emitters can significantly decrease the energy consumption of a drip irrigation system, lowering the capital cost of a solar-powered drip irrigation system [3].

This paper focuses on inline drip emitters (Fig 1), which are embedded inside pipes. Pipes are sold based on emitter spacing and flow rate, depending on crop type and spacing. In contrast, online emitters are sold separately from piping and must be installed by inserting them into the exterior of the pipe one at a time. Because inline drip emitters do not require individual installation, they are generally more popular than online emitter types and account for the significant majority of drip emitter sales [4].

Emitters can be described as pressure compensating (PC) or non-pressure compensating (NPC). PC drip emitters deliver a relatively constant flow rate over a wide range of pressures. The activation pressure is defined as the pressure at which the desired flow rate and flow-compensating behavior begins (Fig. 2). Individual emitters are characterized by their activation pressure (for PC emitters), nominal rated flow rate, and the variation in flow rate from the nominal value. PC drip emitters typically consist of a tortuous flow path and a flexible membrane that deforms to control the flow resistance (Figs. 3A, B). The deformation of

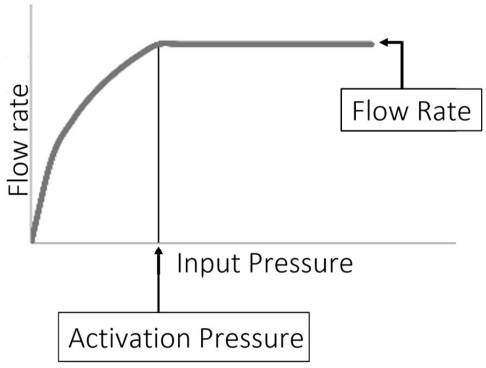

Figure 2. Ideal pressure-compensating behavior. The flow rate through the emitter is a function of two primary flow restrictors: the tortuous path and the membrane interaction with the channel in the lands (Fig. 3). As the input pressure over the membrane increases, the resistance through the channel also increases, resulting in a proportionally lower flow rate. The pressure-compensating mechanism caused by variable flow resistance leads to a constant flow rate at pressures higher than the activation pressure of the emitter.

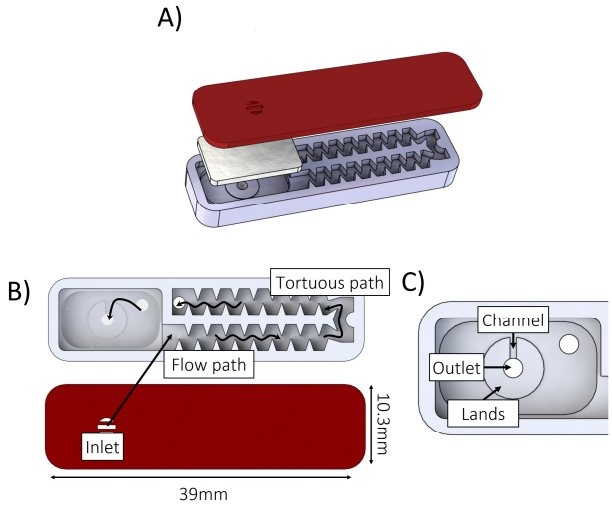

Figure 3. PC inline drip emitter. A) Exploded view of Jain Turbo Cascade 2 L/hr inline drip emitter. B) Inline drippers are embedded in pipes during the manufacturing process. C) Water from the inlet flows to the start of the tortuous path, through the tortuous path, and into a rectangular chamber that has a small channel which provides passageway though the circular lands. A silicone membrane rests on top of the rectangular chamber which deforms under pressure to limit flow. D) The water must flow through the channel in the lands to reach the outlet.

the membrane depends on the input pressure, the pressure underneath the membrane, and atmospheric pressure (Fig. 7). In PC drippers, the design of the tortuous path affects the activation pressure by affecting the pressure differential acting on the membrane and the pressure at which the membrane makes contact with the lands (Fig. 3D). The tortuous path also plays a role in determining the nominal flow rate of the emitter given its resistance in the flow path. NPC drip emitters typically consist solely of a tortuous flow path (Fig. 4A), and thus have a fixed flow resistance. The design of the tortuous path dictates the flow rate behavior as a function of pressure for the device [5].

Understanding the flow behavior through tortuous paths, as well as the coupled fluid-solid mechanics of the flow restriction induced by the flexible membrane, are key components to designing improved emitter technologies. Palau-Salvador et al. [6] showed that computational fluid dynamics (CFD) could be used to accurately simulate flow through tortuous paths in inline emitters. Previous studies on tortuous path behavior have used CFD as a tool to analyze the effects of altering dentate geometry in flow paths [7]. Wei et al. [8] used CFD to characterize the effect of rectangular, trapezoidal, and triangle labyrinth geometries. CFD models, while accurate, can require significant user input to make robust changes to complex geometric structures. CFD models of emitters with labyrinth flow paths and fluid-structure interactions also require significant computational power and time. Some full models of pressure-compensating emitter behavior exist in the literature. Shamshery et al. [9] analytically modeled the pressure versus flow rate behavior of circular PC online emitters that use an orifice rather than a tortuous path for inlet restriction. Zhengying [10] modeled cylindrical inline emit-

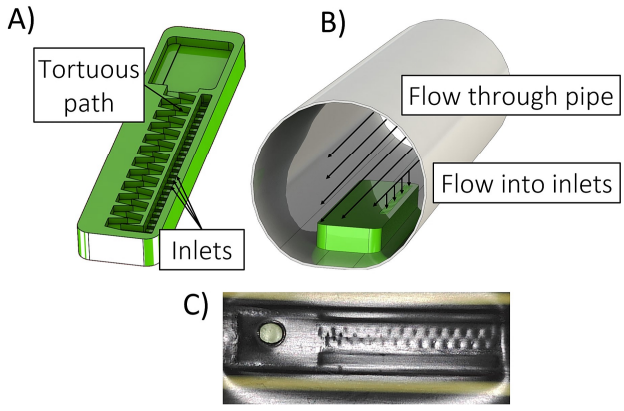

Figure 4. NPC emitters. NPC emitters consist of an array of inlets leading to a tortuous path.

ters with high accuracy using computational fluid structure interactions (FSI) methods. Wang et al. [11] used FSI to model the behavior of circular online drip emitters with high accuracy. The purely analytical model published by Shamshery et al. ([9]), [3]) has very low computational time, but has some error when applied over a range of flow rates [3].

This paper provides a quantitative description of inline PC drip emitter performance, as well as computational and design tools that will enable irrigation engineers to quickly iterate designs. This parametric design theory may lead to improved designs with a lower activation pressure, which can reduce pumping power and capital cost. The model described in this paper has higher fidelity than analytical models described in literature and requires lower computational time than a FSI model of a PC drip emitter. This model includes: a verified CFD model to predict flow behavior through tortuous paths; a method of extracting a pressure scaling parameter from the CFD results to be used in an analytical model; analytical expressions that describe the bending of asymmetric rectangular membranes in inline drip emitters; finite element analysis (FEA) on the shearing behavior of the membrane to calculate total deflection and characterize total flow resistance through the emitter; and analytical expressions that describe the fluid mechanics of duct flows, used to predict the net flow rate out of the emitter. The resulting hybrid computational and analytical model was verified using three distinct commercially available emitter geometries.

The presented model is capable of parametrically describing emitter designs with various flow path architectures. The model also benefits from both the accuracy of computational methods for characterizing complex flow paths and nonlinear mechanics, and the processing speed attainable with analytical expressions.

2 CFD Model of Flow through Tortuous Path

This section describes how CFD was utilized to predict the pressure drop caused by the tortuous path, and determine its loss coefficient. Both the PC and NPC drip emitters investigated in this study use a tortuous path as a flow restrictor. NPC emitters (Fig. 4A), which consist only of an inlet system and tortuous flow path, were used to verify the capability of the CFD model to provide accurate results. Three model geometries were investigated, consisting of single drip emitters with tortuous flow path dimensions equivalent to those of Jain Turbo Excel Plus 0.75, 1.6, and 4 L/hr emitters, which are commercially available products made by Jain Irrigation, Ltd. (Jalgaon, India). These flow rates were selected because they span the range of typical flow rates for NPC drip emitters and have distinct flow paths. The flow behavior was modeled using the ANSYS CFX 16.0 package.

In NPC drippers, the tubing itself provides part of the wall that bounds the flow through the tortuous path (Fig. 4B,C). A fine, controlled mesh was used at the interfaces between the fluid and emitter walls, and between the fluid and piping, to capture the large gradients in flow properties characteristic of boundary layers. The walls were modeled as smooth. A minimum element size on the faces of the fluid in contact with the dripper of $1.8 * 10^{-4}$ m was used to ensure a mesh sufficiently fine to capture the flow behavior. Test runs with smaller element sizes converged yielding the same results as runs with the cited element size. A shear stress transport model (SST) was used for turbulence, as it is suitable for cases in which flow separation and recirculating regions in the flow path are expected [12].

A boundary condition of total pressure was set at the pipe inlet. Total pressure represents the pressure in the irrigation pipe before the flow enters the emitter, and was used as an independent variable. The inlet flow was defined as normal to the pipe inlet with medium turbulence. A boundary condition of average atmospheric static pressure of zero gauge pressure was set at the emitter outlet.

In the manufacturing facility of Jain Irrigation Ltd., polyethylene tubing is heat-formed around a moving line of inline emitters, which are bonded to the inside surface of the tubing at set length increments. The heat-forming process results in portions of the tubing being pushed into the tortuous path, altering the flow path dimensions (Figure 4C). This obstruction was modeled as a $1.5 * 10^{-4}$ m reduction in the depth of the tortuous path, based on measurements on Jain emitters embedded in pipes.

A visualization of the flow through the emitter as computed by the CFD model (Fig. 5) is consistent with images published by Jain Irrigation [13] and Wei [8]. The bulk of the flow moves through the center of the flow path. Lower velocity recirculation zones are formed in the teeth of the labyrinth. Studies on other labyrinth channels have found that recirculation zones affect the likelihood of emitter clogging [8].

Results of the CFD model were compared to measured emitter flow rates (Fig. 6) under controlled pressure for the 0.75, 1.6, and 4 L/hr Turbo Excel Plus driplines. The pressure was measured in the pipe near the inlet of the dripper using a Dwyer DPGA Series digital pressure gauge ($+/-$ 0.1 bar). The flow rate out of the dripline was measured using a graduated cylinder ($+3$ mL) and timer ($+$ 3 s). Figure 6 also shows the geometry of each emitter and reports the 95% confidence interval for the experimental measurements. The flow rate behavior as a function of pressure predicted by the CFD model reliably overlapped with the 95% confidence interval of the experimental data, validating the CFD model predictions within the tested pressure range.

3 Scaling Parameter Based on Tortuous Path Geometry

The primary objective of this paper is to develop an accurate, computationally efficient model of PC emitters. It is difficult to experimentally verify a CFD model of tortuous paths in PC emitters directly because the overall flow behavior is influenced by both the tortuous path and the silicone membrane

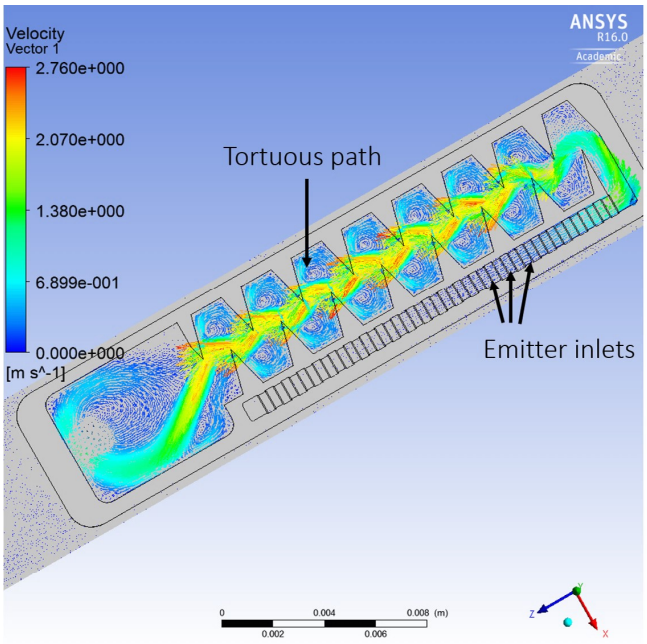

Figure 5. Velocity vectors along the flow path through an NPC drip emitter rated at 1.6 L/hr, computed using ANSYS CFX. Flow enters the emitter through a row of rectangular inlets that lead directly to the tortuous path.

pressure-compensating mechanism (Fig. 3). Therefore, these two flow resistances were investigated separately. The tortuous path model is described here. A CFD model that accurately predicts flow behavior for NPC emitters can be extended to the tortuous path in PC emitters because the design of tortuous paths and the placement of the path in the overall emitter architecture is similar between NPC and PC emitters (Figs. 3 and 4). The verified tortuous path CFD model was therefore used to characterize flow resistance through tortuous paths equivalent to those in Jain PC Turbo Cascade 1.1 L/hr, 2 L/hr and 3.8 L/hr emitters.

The flow through the tortuous path is expected to be turbulent [8]. As such, the flow rate Q can be expressed as a function of the pressure drop $P_2 - P_1$ through the path and a flow resistance parameter K_1 by

$$Q = \frac{\sqrt{P_2 - P_1}}{K_1}, \tag{1}$$

where P_1 is the pressure at the inlet of the emitter, and P_2 is the pressure at the end of the tortuous path. For a PC emitter, where there is a second pressure drop caused by the silicone membrane pressure compensating mechanism (Figure 7), P_2 can be calculated iteratively using Eq. 1 and

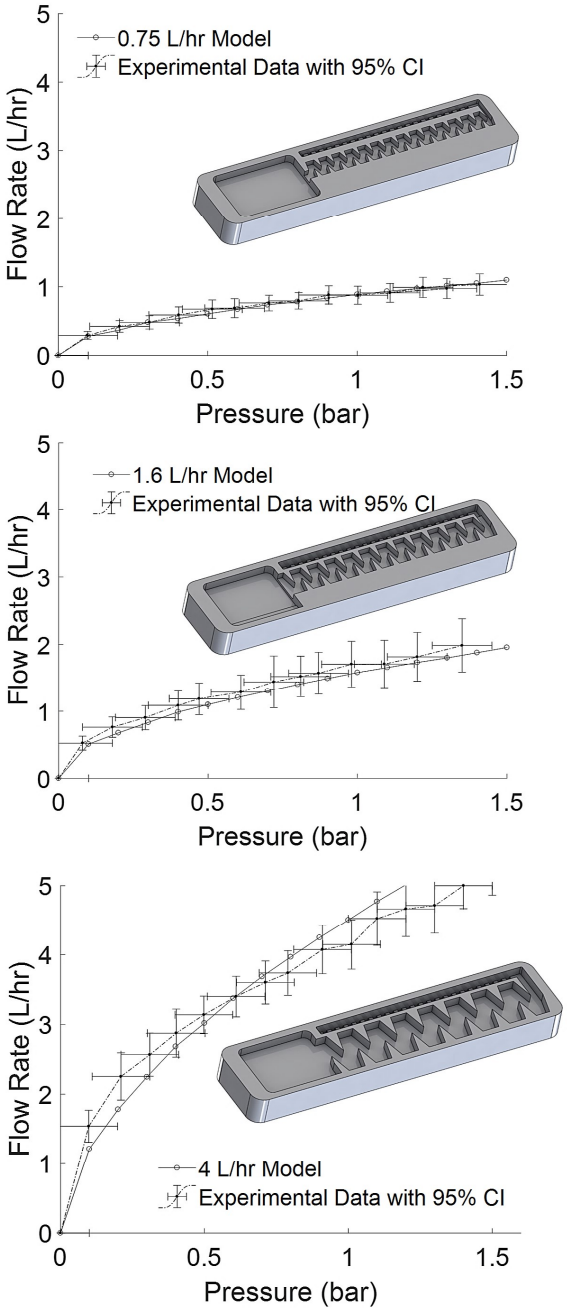

Figure 6. Flow rate as a function of pressure predicted by the CFD model (circles) compared to experimental for three NPC emitters. The CAD model shown with each plot is of the corresponding emitter.

$$P_2 - P_a = \frac{1}{2}(\rho)(K_{mt})Q^2, \tag{2}$$

where P_a is atmospheric pressure at the dripper outlet, K_{mt} is the

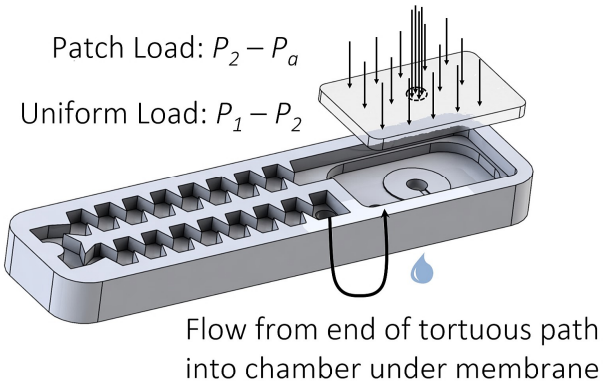

Figure 7. Membrane loading in a PC drip emitter. Water enters the dripper at pressure P_1, flows through the tortuous path and drops to pressure P_2, and then flows into the rectangular chamber underneath the membrane, over the lands and through the channel, and out to atmospheric pressure P_a. The pressure differential applied to the membrane causes it to deflect and control the flow resistance.

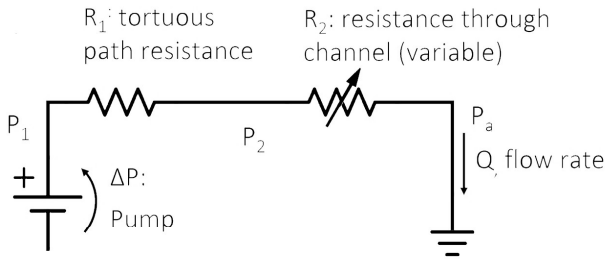

Figure 8. The flow rate through a PC emitter is a function of two primary flow restrictors: the tortuouspath and the membrane interaction with the channel in the lands(Fig. 1). As P_1 increases, the resistance through the channel R_2 also increases, resulting in a proportionally lower flow rate.

total flow resistance under the membrane, and ρ is the density of water, taken as 1000 kg/m^3. The procedure for determining K_{mt} is discussed later in the paper. The process for calculating P_2 is analogous to using the voltage divider rule in an electrical circuit (Figure 8), given the total applied potential (in this case $P_1 - P_a$) and the resistance of two resistors in series (with the modification that the second pressure drop is proportional to Q^2).

To measure P_2, a virtual sensor was placed at the end of the tortuous path in the CFD model, immediately before entering the PC chamber with the channel and lands. The simulation was run for sixteen distinct values of P_1, ranging from 0.1 to 1.6 bar, for each path geometry. The calculated tortuous path flow resistance and corresponding standard deviation for each emitter geometry are summarized in Table 1. It was found that the tortuous path resistance, K_1, depends solely on the geometry of the tortuous path; it does not vary significantly with the pressure potential applied over the path $P_1 - P_2$ or flow rate Q, as expected for a turbulent, inertially-dominated flow.

The standard deviations of the tortuous path resistance were very small compared to the average values. The K_1 value for for the 3.8 L/hr emitter was the lowest. This means that the pressure drop in the tortuous path in the 3.8 L/hr emitter is less than the pressure drop in the paths in the 2 and 1.1 L/hr emitters. This result was expected because the path in the 3.8 L/hr emitter is wider and has fewer turns than the paths in other emitters. Despite differences in path geometry, the scaling factor for the 2 and 1.1 L/hr emitters were nearly identical. Though the 2 L/hr emitter has a wider flow path and fewer turns than the 1.1 L/hr emitter, it had significantly more recirculating flow than the 1.1 L/hr emitter. Dai et. al. found that vortices and flow separation near bends in tortuous channels lead to higher pressure drops [14]. This phenomena would account for similar tortuous path resistances for the 1.1 L/hr and 2 L/hr flow paths, despite distinct geometries.

Table 1. Summary of average tortuous path flow resistances, K_1, and standard deviations calculated using CFD simulation results for sixteen input pressures for each PC inline emitter path geometry

Emitter flow rate (L/hr)	Average K_1 [(Pa·hr^2)/L^2]	Standard deviation [(Pa·hr^2)/L^2]
3.8	2428	77
2	3245	36
1.1	3239	48

K_1 can be reliably determined by simulating the flow at only one input pressure because the standard deviation between measurements is small. A single value of K_1 can then be used to model the total flow behavior of an emitter. Traditionally, the flow behavior through a tortuous path is characterized by fitting complex polynomial or exponential functions to a curve of flow rate as a function of pressure [10], [15]. Generating a full curve requires significantly more computational time than simulating the flow at only a single point.

4 Description of Pressure-Compensating Behavior

In a PC emitter, after the flow passes through the tortuous path, it enters into the pressure compensating chamber underneath a silicone membrane (Fig. 7). To pass from the tortuous path into the chamber, the flow moves through a passage between the emitter and pipe that connects the end of the tortuous path to the chamber underneath the membrane.

Due to the tortuous path, the water enters the chamber underneath the membrane at a pressure P_2, which is lower than the input pressure P_1 above the membrane (Fig. 7). The outlet is open to atmospheric pressure P_a. The resulting pressure differentials across the membrane cause it to deflect (Fig. 9). As P_1 increases, the membrane deflects farther and farther into the chamber until it hits the lands at pressure P_L. For pressures greater than P_L, the flow must move through the small channel that passes through the lands to reach the emitter outlet (Fig. 3C).

The increasing flow resistance as the membrane deflects causes the pressure P_2 under the membrane to increase. The pressure drop through the channel P_2 - P_a increases proportionally to P_1. An increase in flow resistance through the channel regulates the flow rate as $P_2 - P_a$ increases.

In the modeled devices, the membrane has an initial curvature caused by a protrusion on the cap of the emitter. The distance between the membrane and the lands was estimated as the distance between the center of the membrane and the lands.

After the membrane touches the lands, the lands apply a contact force on the membrane. For $P_1 > P_L$, the membrane deforms into the channel. The magnitude of obstruction is primarily a function of the input pressure P_1. At higher input pressures, the magnitude of deformation is greater, leading to a higher flow resistance in the channel. The emitter pressure compensates because the flow resistance is greater for higher input pressure - that is, for a range of pressures beginning with the activation pressure, P_{act}, water leaves the emitter at a constant flow rate (Fig. 2).

4.1 Membrane bending for $P_1 < P_L$

Before the membrane touches the lands, the loading on the membrane can be modeled as the linear superposition of a uniform load and a patch load (Fig. 10). The pressure P_1 is applied uniformly over the top surface of the membrane. In regions where there is fluid of pressure P_2 beneath the membrane, the loading is $P_1 - P_2$. In regions where there is no fluid at P_2 beneath the membrane, the loading is $P_1 - P_a$. This loading can be represented by the superposition of a uniform load $P_1 - P_2$ over the entire membrane and a patch load $P_2 - P_a$ over the portion of the membrane that is not in contact with fluid at pressure P_2. (Fig. 7).

The membrane was modeled as a rectangular plate with four simply supported edges. The dimensions of the membrane were taken as the distances between each set of parallel supports. The membrane was modeled after the membranes used in the 1.1, 2, and 3.8 L/hr Turbo Cascade emitters, which have length a of 7.0 mm, width b of 12.0 mm, and thickness h of 1.2 mm. All emitter dimensions given in this paper were measured using hand calipers ($+/-$ 0.1 mm).

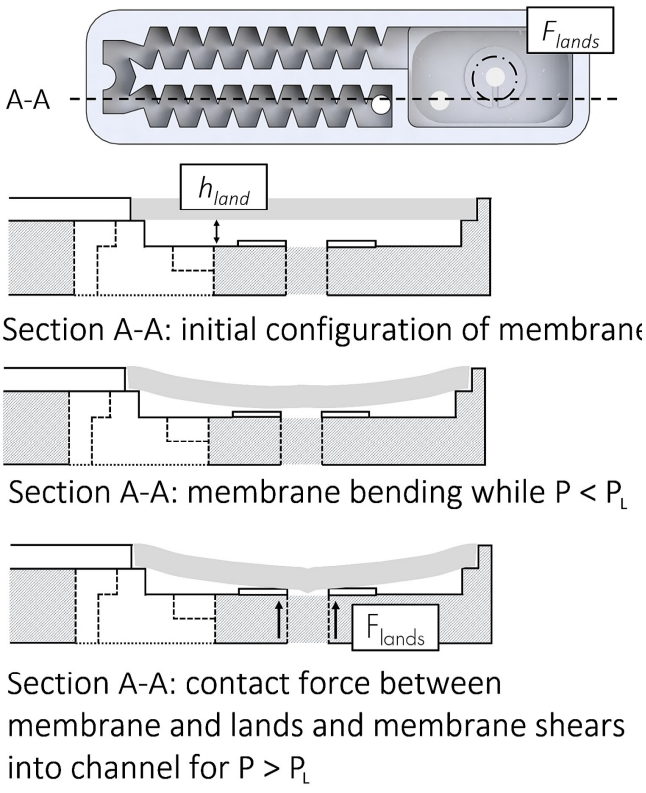

Figure 9. Cross-sectional view of the pressure-compensating chamber in an inline drip emitter.

The material properties of the membrane were found using correlations between material properties and material hardness for rubbers [16]. To find the hardness of the membrane, a type A durometer was pressed into a stack of membranes resting on a hard surface. After recording the measurement, an additional membrane was added to the stack and the measurement was repeated. This process was repeated until adding an additional membrane to the stack did not change the recorded hardness. The final stack consisted of eight membranes. This procedure was used to ensure that the presence of the hard surface underneath the membranes did not affect the measured hardness value. The measurement process was repeated three times, and it was found that the membrane had a hardness of 52 $\pm$ 1 degrees.

The Young's modulus of a material in MPa, E is related to the material hardness, H_A by [16]

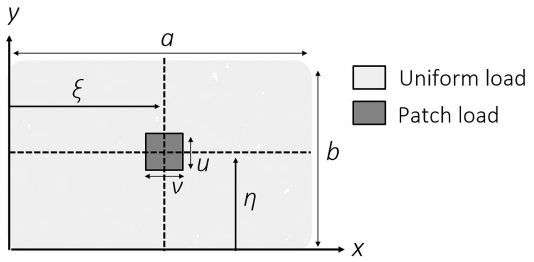

Figure 10. Loading on membrane for $P_1 < P_L$. Before the membrane touches the lands, the loading on the membrane can be modeled as the superposition of a uniform load and a patch load.

$$E = (15.75MPa + 2.15MPa * H_A)/(100 - H_A) \tag{3}$$

This expression gives a Young's modulus E of 2.66 ± 0.18 MPa. For a neo-Hookean material, the shear modulus, G, is one third of E, 0.89 MPa. Using these values of E and G, the Poisson's ratio of the membrane, ν, was calculated to be 0.488. [16].

The deflection of the membrane due to the uniform load, $w_{uniform}$, can be modeled using a Navier double series solution [17],

$$w_{uniform}(x,y) = \frac{16(P_1 - P_2)}{D\pi^6}\left(\frac{\sin\frac{\pi x}{a}\sin\frac{\pi y}{b}}{(\frac{1}{a^2}+\frac{1}{b^2})^2} + \frac{\sin\frac{3\pi x}{a}\sin\frac{\pi y}{b}}{3(\frac{9}{a^2}+\frac{1}{b^2})^2} + \frac{\sin\frac{\pi x}{a}\sin\frac{3\pi y}{b}}{3(\frac{1}{a^2}+\frac{9}{b^2})^2} + \frac{\sin\frac{3\pi x}{a}\sin\frac{3\pi y}{b}}{9(\frac{9}{a^2}+\frac{9}{b^2})^2}\right). \tag{4}$$

D is the flexural modulus of the membrane, and is given by Equation 5.

$$D = \frac{Eh^3}{12(1-\nu^2)} \tag{5}$$

The portion of the membrane that is not in contact with fluid at pressure P_2 becomes larger as P_1 increases beyond P_L, and the contact area between the membrane and the lands increases. This is because there is no fluid flow under the membrane in regions where the membrane is in contact with the lands. To approximate this effect, the area of application of the patch load was approximated as the average lands diameter, or half the distance between the inner and outer lands. Though the emitter outlet and lands are circular, the patch was approximated as a rectangular patch of the same area as the average lands diamater because the membrane is rectangular and calculations were done in Cartesian coordinates (Fig. 10). The deflection of the membrane due to the patch load, w_{patch}, can also be modeled using a Navier double series solution [17],

$$w_{patch}(x,y) = \frac{16(P_1 - P_2)}{D\pi^6}\left(\frac{\sin\frac{\pi\eta}{a}\sin\frac{\pi\xi}{b}\sin\frac{\pi u}{2a}\sin\frac{\pi b}{2b}\sin\frac{\pi x}{a}\sin\frac{\pi y}{b}}{(\frac{1}{a^2}+\frac{1}{b^2})^2} + \frac{\sin\frac{3\pi\eta}{a}\sin\frac{\pi\xi}{b}\sin\frac{3\pi u}{2a}\sin\frac{\pi b}{2b}\sin\frac{3\pi x}{a}\sin\frac{\pi y}{b}}{3(\frac{9}{a^2}+\frac{1}{b^2})^2} + \frac{\sin\frac{\pi\eta}{a}\sin\frac{3\pi\xi}{b}\sin\frac{\pi u}{2a}\sin\frac{3\pi b}{2b}\sin\frac{\pi x}{a}\sin\frac{3\pi y}{b}}{3(\frac{1}{a^2}+\frac{9}{b^2})^2} + \frac{\sin\frac{3\pi\eta}{a}\sin\frac{3\pi\xi}{b}\sin\frac{3\pi u}{2a}\sin\frac{3\pi b}{2b}\sin\frac{3\pi x}{a}\sin\frac{3\pi y}{b}}{9(\frac{9}{a^2}+\frac{9}{b^2})^2}\right), \tag{6}$$

where η, ξ, u, and v are defined in Fig. 10.

The Navier double series solution is a linear, elastic, small-deflection model, and is valid under the assumptions of Kirchoff's hypotheses for plates [17]. Experiments were used to determine the applicability of Kirchoff plate theory. Material tests were conducted on silicone rubber with material hardness 55 per the ASTM D412 standard [18] with straight specimens. Figure 11 shows the normalized deflection as a function of the normalized applied load, and marks the loading range that corresponds to the operational range of drip emitters. While the material shows strain softening for large loadings, the behavior of the membrane in the range of interest is linear, justifying the use of the Navier double series solutions to model the bending of the membrane in the emitter. Because the models are linear, they can be superimposed. The total deflection of the membrane, w_{bend}, before touching the lands is given by

$$w_{bend} = w_{uniform} + w_{patch}. \tag{7}$$

4.2 Membrane bending for $P_1 > P_L$

For $P_1 > P_L$, the membrane is in contact with the lands (Fig. 9). The lands exert a contact force, w_{conc}, on the membrane,

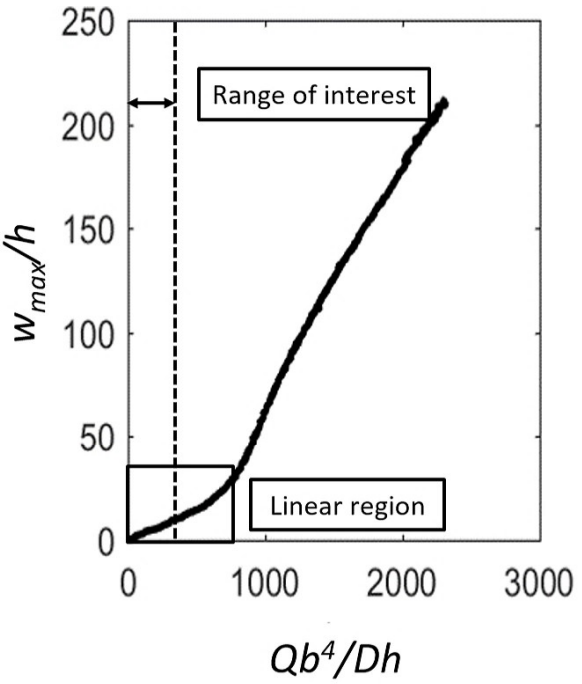

Figure 11. Dimensionless deflection measurements as a function of dimensionless loading for a rubber tensile test silicone rubber of hardness 55, where Q is the loading applied during the test, w_{max} is the measured maximum deflection, b is membrane length, D is the flexural modulus of the membrane, and h is the membrane thickness.

constraining the deflection along the lands. After the membrane contacts the lands, the deflection of the membrane is given by

$$w_{bend} = w_{uniform} + w_{patch} + w_{conc}. \tag{8}$$

The contact force can be approximated as a partial circular line load applied at the inner land diameter. The deflection profile imposed by a circular line load on a rectangular membrane is asymmetric. To the authors' knowledge, no expressions exist in literature suitable for modeling the circular lands force as a line load on a rectangular membrane. The line load along the lands was approximated as a series of concentrated loads (Fig. 12). No loads were applied along the width of the channel. Seventy two concentrated loads were applied along the inner land diameter. Adding additional concentrated loads beyond this number altered the predicted membrane displacement by less than 0.1 %.

The deflection of a rectangular membrane, w_{cont}, at the point (x_i, y_i) due to a concentrated load F_{lands} at (n_i, m_i) is given by the expression [17]

$$w_{cont}(x_i,y_i) = \frac{4F_{lands}}{Dab\pi^4}\Big(\frac{\sin\frac{\pi n_i}{a}\sin\frac{\pi m_i}{b}}{(\frac{1}{a^2}+\frac{1}{b^2})^2}\sin\frac{\pi x_i}{a}\sin\frac{\pi y_i}{b} + \frac{\sin\frac{3\pi n_i}{a}\sin\frac{\pi m_i}{b}}{3(\frac{9}{a^2}+\frac{1}{b^2})^2}\sin\frac{3\pi x_i}{a}\sin\frac{\pi y_i}{b} + \frac{\sin\frac{\pi n_i}{a}\sin\frac{3\pi m_i}{b}}{3(\frac{1}{a^2}+\frac{9}{b^2})^2}\sin\frac{\pi x_i}{a}\sin\frac{3\pi y_i}{b} + \frac{\sin\frac{3\pi n_i}{a}\sin\frac{3\pi m_i}{b}}{9(\frac{9}{a^2}+\frac{9}{b^2})^2}\sin\frac{3\pi x_i}{a}\sin\frac{3\pi y_i}{b}\Big). \tag{9}$$

The deflection at each point (x_i, y_i) of interest along the lands is known based on the geometry of the emitter. Let **n** and **m** be matrices that store the $x-$ and $y-$ locations respectively of each point at which a concentrated load is applied. The vectors designating points at which the displacement is calculated, **x** and **y** are identical to the vectors designating points at which the concentrated loads are applied, **n** and **m**. At each point (x_i, y_i) along the line load, the total applied line load is the sum of the effects of each concentrated load in the matrix [**n m**]. In a more general case, Eqn. 9 could be use to calculate the affect of a series of concentrated loads at position [**n m**] at any point (x, y) in the domain.

The loadings due to the fluid pressure differentials $P_1 - P_2$ and $P_1 - P_a$ cause the membrane to deflect downwards. When the membrane makes contact with the inner lands diameter, the line load applied by the lands prevents the membrane from deflecting farther downward. The line load applies a force in the direction opposed to the fluid pressure loading. The magnitude of the applied line load is such for $P_1 > P_L$, the total deflection at a point (x_i, y_i) along the lands must equal the distance between the surface supporting the membrane and the top surface of the lands, h_{land} (Fig. 9).

$$h_{land} = \sum_{j=1}^{72} w_{cont}(n_j, m_j)|_{x_i,y_i} + w_{bend}(x_i, y_i). \tag{10}$$

The prescribed deflection, $h|_{(x_i,y_i)}$ of the membrane at the point (x_i, y_i) due to the concentrated loads is then given by

$$h|_{(x_i,y_i)} = h_{land} - w_{bend}(x_i, y_i). \tag{11}$$

Assuming that the applied force does not vary with the point of application along the lands, the force can be solved for directly using matrix operations. Let **x** and **y** be 72 x 1 matrices that store

the x and y locations of the points along the lands at which the deflection will be constrained. Using Eqn. 10, the relationship between the applied force, F_{lands} in Pa·m^2 and the known deflection, $h_{(\mathbf{x},\mathbf{y})}$ can be written as

$$F_{lands} \cdot \mathbf{W} = \mathbf{h}_{(\mathbf{x},\mathbf{y})}. \tag{12}$$

$\mathbf{W}$ is a 72 x 1 matrix with units $\frac{1}{Pa \cdot m^3}$ given by the expression

$$\begin{aligned}\frac{4}{Dab\pi^4}\Big(&\sum_{j=1}^{72}\Big(\frac{\sin\frac{\pi n_j}{a}\sin\frac{\pi m_j}{b}}{(\frac{1}{a^2}+\frac{1}{b^2})^2}\Big)\sin\frac{\pi\mathbf{x}}{a}\sin\frac{\pi\mathbf{y}}{b}\\ &+\sum_{j=1}^{72}\Big(\frac{\sin\frac{3\pi n_j}{a}\sin\frac{\pi m_j}{b}}{3(\frac{9}{a^2}+\frac{1}{b^2})^2}\Big)\sin\frac{3\pi\mathbf{x}}{a}\sin\frac{\pi\mathbf{y}}{b}\\ &+\sum_{j=1}^{72}\Big(\frac{\sin\frac{\pi n_j}{a}\sin\frac{3\pi m_j}{b}}{3(\frac{1}{a^2}+\frac{9}{b^2})^2}\Big)\sin\frac{\pi\mathbf{x}}{a}\sin\frac{3\pi\mathbf{y}}{b}\\ &\sum_{j=1}^{72}\Big(\frac{\sin\frac{3\pi n_j}{a}\sin\frac{3\pi m_j}{b}}{9(\frac{9}{a^2}+\frac{9}{b^2})^2}\Big)\sin\frac{3\pi\mathbf{x}}{a}\sin\frac{3\pi\mathbf{y}}{b}\Big),\end{aligned} \tag{13}$$

and $\mathbf{h}_{(\mathbf{x},\mathbf{y})}$ is a 72 x 1 matrix defined as

$$\begin{bmatrix} h|_{(x_1,y_1)} \\ h|_{(x_2,y_2)} \\ \vdots \\ h|_{(x_{72},y_{72})} \end{bmatrix},$$

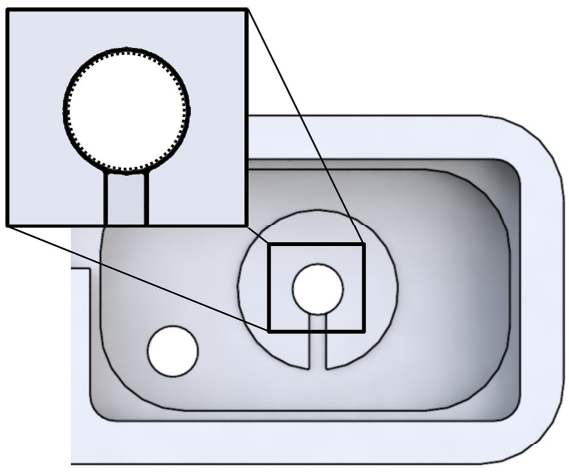

Figure 12. Contact force between membrane and lands. The contact force between the membrane and lands was modeled as a series of concentrated forces. Each dot in the dotted line represents a location at which a concentrated force was applied.

where the value of each element $h|_{(x_i,y_i)}$ is given by Eqn. 11. The value of F_{lands} is then given by

$$F_{lands} = \mathbf{W} \setminus \mathbf{h}_{(\mathbf{x},\mathbf{y})}. \tag{14}$$

Because W is a rectangular matrix with more rows than columns, the system is overdetermined and F_{lands} is the least-squares solution. In this calculation, F_{lands} was assumed to have the same magnitude at each point along the lands. Physically, the value of F_{lands} may vary with the point of application of the force along the circumference of the lands. To evaluate the validity of the solution, the approximated quantity $F_{lands} \cdot \mathbf{W}$ was compared to the known matrix $\mathbf{h}_{(\mathbf{x},\mathbf{y})}$. $F_{lands} \cdot \mathbf{W}$ was found to be within 0.0015 % of $\mathbf{h}_{(\mathbf{x},\mathbf{y})}$, validating the assumptions made in the analysis. Figure 13 illustrates the deflection of the membrane due to $w_{bend}, \Sigma w_{cont}$, and the total bending due to w_{bend} and Σw_{cont} for a representative 2 L/hr emitter. The addition of the contact force along the lands changed the shape of the deflection profile. Inside the inner diameter of the lands, the membrane curved upwards slightly due to application of the contact force.

While the expressions derived in this section was applied to a circular line load representing a circular support, the matrix formulations can be applied to a support of generic shape. The expressions are applicable to a line or patch load of any arbitrary shape along which there is a known deflection applied onto a rectangular membrane. Calculating the magnitude of the line load and the associated deflection analytically allow for a rapid calculation of flow resistance changes with geometry changes.

4.3 Membrane obstruction into channel for $P_1 > P_L$

After the membrane contacts the lands, it begins to deflect into the channel. The total deflection of the membrane is the greatest at the center of the membrane near the outlet of the emitter, where the patch load is applied. As the applied pressure increases, the membrane deforms further into the channel. The deformation of the membrane into the channel effectively increases the length of the channel through which the flow must pass. As the input pressure increases, the cross-sectional area of the flow passage also decreases. This is the primary source of the increasing flow resistance that causes pressure-compensating behavior.

Shamshery and Winter [9] previously used thick beam theory to model the shearing behavior of a section of membrane into the channel of online PC drip emitters. They linearly superimposed the predicted bending and shearing deformations for the thick beam with the bending deformation of the membrane. In this study, the thick beam model was used to provide a cross-sectional profile as a basis to apply correction functions derived from finite element analysis. The thick beam model alone does not provide an accurate prediction of the magnitude of membrane

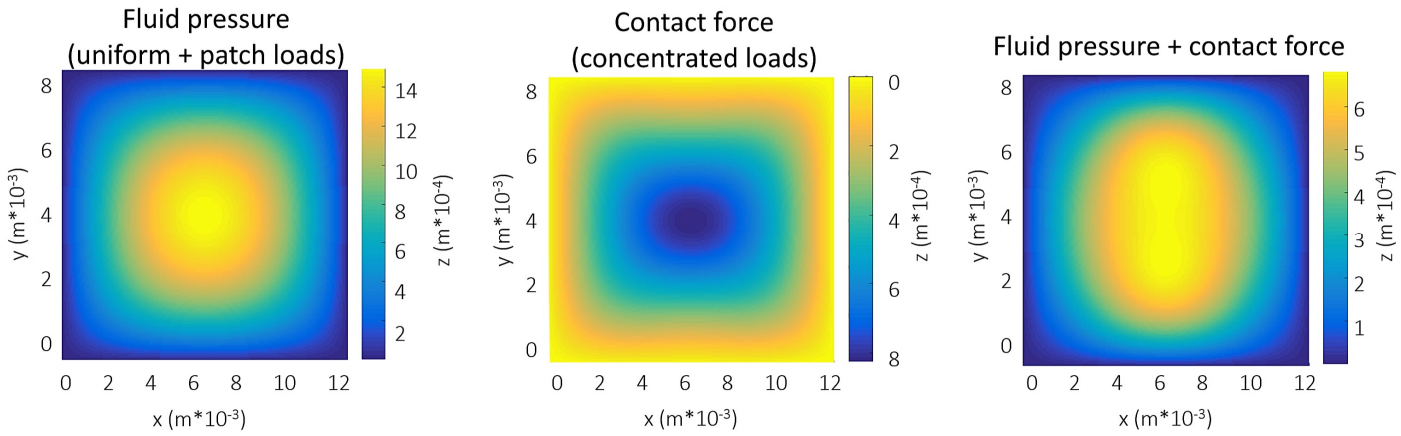

Figure 13. Bending deflection visualization immediately after the membrane touches the lands in a 2 L/hr inline drip emitter. The total force acting on the membrane is the sum of the applied fluid pressure and the contact force exerted by the lands. The inner and outer land diameters of the modeled geometry were 0.0012m and 0.00476m, respectively.

deflection because the span/depth ratio of the portion of the membrane over the channel is small and the deflection profile is not uniform through the width of the beam (the length of the channel) [19]. This study used finite element analysis to scale the profile to more accurately model the magnitude of the obstruction.

The finite element model was used to develop functions to describe the magnitude of membrane deformation into the channel and the fraction of the channel into which the membrane deformed as a function of pressure. A mechanical model to study the interaction of the membrane with the lands was constructed in the ANSYS 18.1 static structural package. The membrane was modeled as a two-dimensional, first order Neo-Hookean solid. The model used a rectangular mesh of shell elements. The contact between the membrane and the lands was modeled as frictional with a friction factor of 0.2. Gauss point detection was used between the membrane and lands structure. For $P_1 < P_L$, the maximum deflection predicted by the finite element model was within 10 % of the maximum deflection predicted by Eqn. 7.

A two-dimensional model of the interactions between the membrane and the lands is an approximation because the channel dimensions are comparable to the thickness of the membrane. A two-dimensions model may underpredict the stiffness of the

membrane in the region over the channel after the membrane touches the lands. A two-dimensional model also does not account for the bulk deflection of the membrane in response to the force applied by the lands structure, which may be significant for a membrane of this shape [16]. However, the two-dimensional model has significantly lower computational time than a three-dimensional model. Additionally, three-dimensional models of rubbers in finite element analysis are not easily implemented and tend to be error prone [16]. The finite element model captures the changing magnitude and area of application of the contact force between the lands and the membrane, an interaction not easily modeled using analytical expressions. The finite element model did not model the contact interactions between the channel bottom and the membrane. From experiments it was known that the bottom of the membrane does not touch the channel within the range of pressures studied. A limiter was applied on the maximum membrane deflection to ensure a channel height of at least 0.01mm.

The complete system model with fluid-structure interactions was validated using experimental data. The structural model was not validated separately because experimental data could not be collected on the magnitudes of structural deformation in the channel in the emitter. The approximations in the structural model described above may contribute to the errors in the system model.

In the two dimensional analysis, the deformation of the membrane is modeled as constant throughout the thickness of the membrane. For high values of P_1, it is not expected that this will be true in a real emitter. The deflection of the bottom surface of the membrane, which determines the flow resistance through the emitter, will be less than the deflection of the midplane of the membrane as the contact force increases. Because of these approximations, the finite element model likely over-predicts deformation into the channel for high input pressures.

The deflection of the membrane in the finite element model was sampled at 0.1 mm increments along the length of the channel. A nodal pressure $P_1 - P_a$ was applied at the center of membrane over a circle with diameter equal to the average lands radius, and a nodal pressure $P_1 - P_2$ was applied over the rest of the membrane. P_2 is initially unknown, but can be calculated iteratively using an initial guess that is refined using the values calculated from the complete hybrid model.

Due to the high flow resistance in pressure compensating emitters, $P_1 - P_2$ was expected to be approximately an order of magnitude lower than P_1 for $P > P_{act}$, or, on the order of 0.1 bar. Thus, the first iteration of the finite element model was run with $P_1 - P_2$ equal to 0.1 bar. The resulting scaling functions were used in the complete hybrid model to calculate Q, as well as a new prediction for the value of P_2 at each input pressure. The new P_2 predictions were then used as inputs in the finite element model. This process was repeated until further refinements on the values of P_2 had no affect on the predicted flow rate, Q. After two iterations of the finite element model, the final predicted values of Q for the 2 L/hr emitter converged with a maximum error of 10.6% and an mean error of 3.1% (Fig. 14).

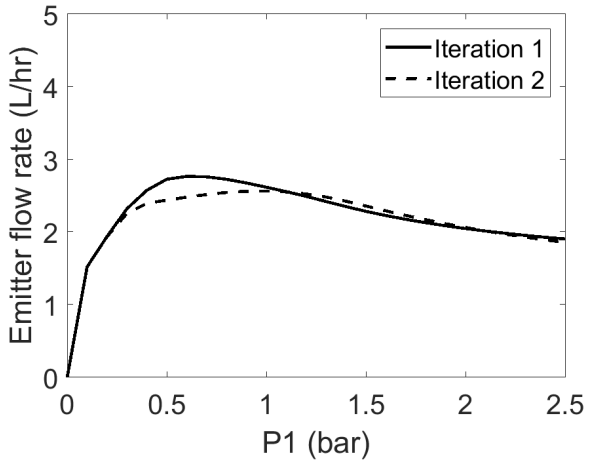

Figure 14. The predicted flow rate of the 2 L/hr emitter converged within two iterations of the scaling functions over P_2

The fraction of the channel covered by the membrane rose with P_1 over the entire range (Fig. 16). The pressure at which the membrane made contact with the lands corresponds to a marked change of slope in the maximum deflection along the channel as a function of pressure. Exponential functions were fit to describe the maximum deflection and channel fraction as a function of P_1. The maximum deflection into the channel, $w_{ch,max}$ was used to scale a normalized deflection profile for a clamped thick beam [20],

$$w_{normalized}(x) = (2.3269 * 10^{14})x^4 - (2.3269 * 10^{11})x^3 + (5.6525 * 10^7)x^2 + 824.2173x - 0.0077. \quad (15)$$

The deflection along the length of the channel decayed parabolically from its maximum value at the inner land radius, l_{ri}. A parabolic function was defined with a value of 1 at the inner land diameter and value of 0 at the point where the membrane first contacts the lands, as defined by the channel fraction. This function defines a scaling function, $S_p(y)$, which is the ratio of the deflection at a given point along the channel to the maximum deflection along the channel, for a constant input pressure P_1. Thus, the deflection profile into the channel (Fig. 15), w_{ch}, at a given point along the channel, y, is given by

$$w_{ch}(x) = (w_{ch,max} - h_{lands}) * S_p(y) * w_{normalized}(x), \quad (16)$$

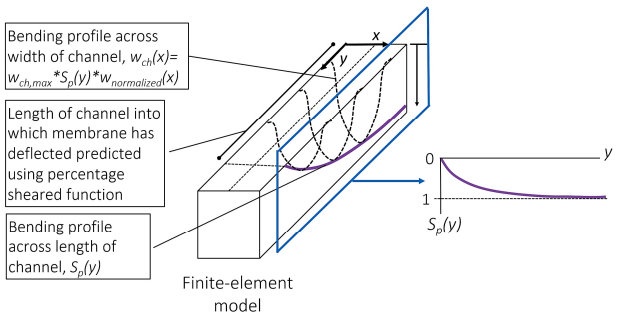

Figure 15. The hybrid-analytical model incorporates results from FEA simulations using scaling relationships. The maximum deformation of the membrane into the channel and the length of the channel into which the membrane has deformed are predicted from FEA simulations using scaling relationships 16. The profile across the width of the beam, $w_{normalized}(x)$ is found from Eq. 15.

The exponential fit functions for the maximum deflection along the channel and channel fraction as a function of input pressure (Fig. 16) were generated using increments of 0.1 bar for P_1 and have R^2 values of 0.99 and 0.96 respectively. Sampling at 0.1 bar intervals between 0.2 and 0.6 bar and 0.4 bar interval between 0.6 and 2.2 bar did not lower the R^2 value of the fit functions, but reduced the required computational time by approximately 60 %. A higher sampling resolution was used for lower pressures where the maximum deflection changes more rapidly. The scaling functions for the 1.1 L/hr and 3.8 L/hr emitters were found using this sampling method.

To find the scaling factors for the 1.1 L/hr and 3.8 L/hr emitters, the final values for P_2 from the 2 L/hr emitter analysis were used in the first iteration of the new finite element analysis. Due to the more accurate initial input for P_2 compared to the initial values of 0.1 bar used for the 2 L/hr emitter, the flow rate predicted by the hybrid model for the 1.1 L/hr emitter and the 3.8 L/hr emitter converged with one iteration of scaling functions from finite element analysis.

5 Flow Modeling

When the flow enters the section under the membrane, there are two paths it can take to reach the channel, flow paths A and B in Fig. 17A. Due to the much longer flow path, the flow resistance through flow path B is much higher than the resistance through A, and therefore flow through flow path B was neglected in this analysis. Path A can be sub-divided into two zones, as

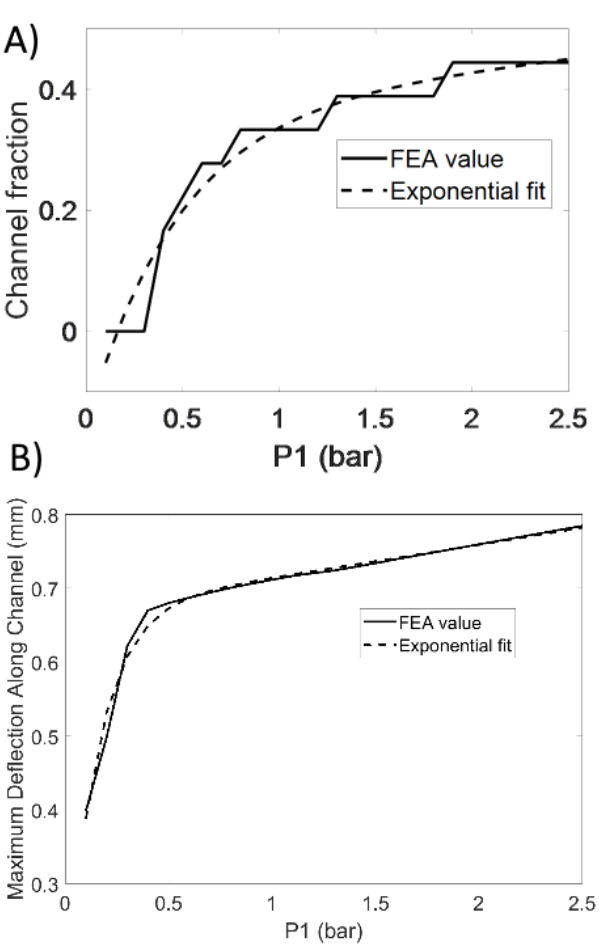

Figure 16. Scaling functions describing membrane obstruction into channel. Polynomials were fit to results from the FEA model to create expressions for a scaling factor and percent channel shearing as a function of pressure. The scaling functions at the final iteration for the 2 L/hr emitter geometry are shown here. A) The channel fraction, or percentage of the channel into the which the membrane had sheared, at each input pressure. B) The maximum deflection along the channel at each input pressure.

shown in Fig. 17B.

The height of the passage in zone 1 was calculated using the analytical expressions for membrane bending, Eqn. 7 and Eqn. 8. The height of the passage in zone 2 was calculated using the functions derived from finite element analysis, as per Eqn. 16. Zone 1 was divided into 10 subsections and zone 2, the dominant flow resistance, was divided into 50 subsections. The profile of the membrane bending across the width of the section (the dimension parallel to the membrane width b) was calculated in each section and a polynomial was fit to match the bending profile. The hydraulic diameter in each subsection was calculated by integrating to find the area through each section and the perimeter

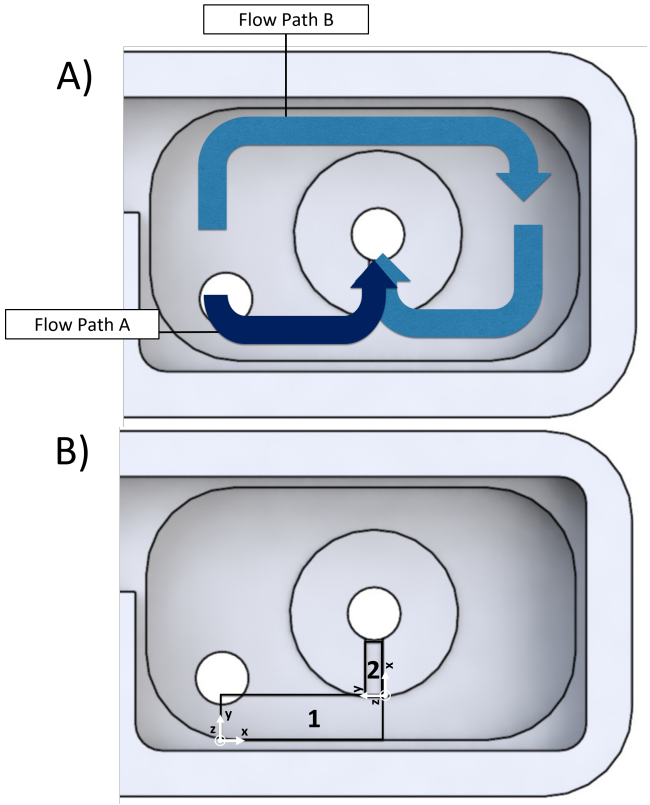

Figure 17. A: The flow entering the passage under the membrane can go through path A or path B. Because flow resistance through path B is much higher than the flow resistance through path A, the flow resistance of path B was neglected in the analysis. B: The flow resistance through Flow Path A was calculated as the sum of the flow resistances in Zones 1 and 2

enclosing each subsection. The frictional loss in each subsection was calculated using Eqn. 17. The frictional losses through a duct are given by

$$K_{fric} = \frac{fL}{D_h}. \tag{17}$$

In this expression f is the friction factor, L is the length of the duct, and D_h is the hydraulic diameter of the duct. The total frictional loss is equal to the sum of the frictional loss in each subsection. The variables f and D_h depend on the cross-sectional profile and area of the duct and were calculated by integrating along the duct profile, defined by the expressions for the bending and shearing of the membrane described earlier. The parameter f was calculated implicitly using the Colebrook interpolation formula [21] using an absolute roughness of 0.0015 mm, estimated from the literature for drawn plastic pipes [22], [23],

$$\frac{1}{f^{\frac{1}{2}}} = -2.0\log\left(\frac{\varepsilon/D_h}{3.7} + \frac{2.51}{Re_{D_h} f^{\frac{1}{2}}}\right). \tag{18}$$

The flow velocity can be calculated using the properties of the fluid and the losses through the channel [21], [9], using

$$P_2 - P_a = \frac{1}{2}\rho K_{fric}(v_{ave})^2 + \frac{1}{2}\rho(v_{ave})^2 \Sigma K_{minorloss}. \tag{19}$$

$K_{minorloss}$ are the minor loss coefficients for irregularities in the flow path geometry. In this model, minor losses for the flow moving out of the labyrinth, into the chamber underneath the membrane and through the outlet were accounted for. The magnitude of $K_{minorloss}$ depends on the diameters of the passageway before and after the change in duct dimension and can be estimated using the expression [21]

$$K_{minorloss} = \left(1 - \frac{D_1^2}{D_2^2}\right)^2. \tag{20}$$

Eqn. 19 was derived from the Navier-Stokes solution for one dimensional, steady-state, fully developed flow. Due to the varying dimensions of the flow path, the flow through the emitter paths is neither one dimensional nor fully developed. These expressions can be used as a reasonable approximation where locally fully developed flow can be assumed. Following [24], the approximation for locally fully developed flow is reasonable [24]when the Navier-Stokes equations

$$\frac{\partial(\rho u_i)}{\partial t} + \frac{\partial[\rho u_i u_j]}{\partial x_j} = -\frac{\partial p}{\partial x_i} + \frac{\partial \tau_{ij}}{\partial x_j} + \rho g_i, \tag{21}$$

can be reduced to

$$\frac{\delta P}{\delta x} = \mu \frac{\delta^2 U}{\delta z^2} \tag{22}$$

$$\frac{\delta P}{\delta y} = 0 \tag{23}$$

$$\frac{\delta P}{\delta z} = 0. \tag{24}$$

A self-consistency check was performed after evaluating the flow rate using Eqn. 19 at input pressures of 0.1 bar and 1 bar. For the locally fully developed flow assumption to be valid, the relative magnitude of the neglected terms in Eqn. 21 must be small in comparison to the retained terms when moving to Eqns. 22-24. The first term is Eqn. 21 is negligible because the flow is steady state at each input pressure. In zone 1, it was estimated that V, the flow in the y direction (Fig. 17) was on the order of one-tenth of the flow along the x direction, because the flow resistance through flow path B was approximately ten times the flow resistance through flow path A. The order of U was found using the calculated flow rate out of the emitter and the average flow path dimensions. Conservation of mass was used to estimate the order of W.

The self-consistency check suggested that the approximation of locally fully developed flow was most valid in zone 2 for $P > P_L$. Inertial contributions of the flows in the x and z directions could be significant, particularly in zone 1. Because the flow resistance through zone 2 is significantly higher than the flow resistance through zone 1, deviations from the approximation of locally fully developed flow in zone 1 will introduce less error in the analysis. The analysis suggested that the approximation of locally fully developed flow can be used to analyze the relative flow behavior through emitters of different geometries, but it may result in some error in the model, particularly for low pressures.

6 Results

The hybrid computational-analytical model was used to predict flow rate as a function of pressure for three models of the Turbo Cascade PC emitter (1.1, 2.0, and 3.8 L/hr). The emitter flow rates as a function of pressure were measured by attaching samples of the drip tubing to an adjustable pressure water source. Pressure and flow rate were measured as described in Section 2. Figure 18 compares the measured flow rates as a function pressure to the hybrid model predictions, indicating 95% confidence intervals for measured values and shows the geometry of each emitter. As a comparison, data provided in the product datasheet by Jain Irrigation Ltd. [25] are also included.

The model slightly overpredicted the experimental data for the 1.1 L/hr emitter. However, the model was consistent with experimental data for the 2.0 and 3.8 L/hr emitter over most of the tested pressure range. The flow rate predicted by the model was reasonably close to the datasheet values published by Jain Irrigation for the 1.1 L/hr emitter and was very close to the published values for the 2.0 and 3.8 L/hr emitters. The trends shown in the model match the trends of the experimental data. For the 1.1 L/hr emitter, the average error between the model and the experimental data was 10.7% and the average error between the model and datasheet values was 18.1%. For the 2.0 L/hr emitter, the average error between the model and the experimental data was 4.7% and the average error between the model and datasheet values was 6.7%. For the 3.8 L/hr emitter, the average error between the model and the experimental data was 11.0% and the average error between the model and datasheet values was 8.9%.

The activation pressure of an emitter was defined as the pressure at which the flow rate was within 10% of the average flow rate. The calculated activation pressures and average flow rate are presented in Table 2. For consistency with the available experimental dataset, the activation pressure predicted by the model was calculated for the range 0-1.5 bar. The model predicted the flow rate through each emitter over the range of pressures and the activation pressure of each emitter with reasonable accuracy.

Experimental data was collected to confirm the accuracy of the published data and to determine a confidence interval. The 95% confidence interval of the experimental data was consistent with the published data, indicating that the published data should be sufficient to validate the predicted model flow rate. The experimental data was used to evaluate the accuracy of the predicted activation pressure because the activation pressure in the published data is reported with a unknown safety factor. The published activation pressure is 0.5 bar for all three emitters [25].

The model had higher fidelity for emitters with higher flow rates. Similar absolute errors between the model predictions and experimental and datasheet curves were similar for all emitters lead to larger relative errors for lower flow rates. Overall, the model has sufficient accuracy to characterize the relative performance of drip emitters given a defined architecture over a range of flow rates.

7 Discussion

The behavior of P_2 can provide some insight into the behavior of a drip emitter. As P_1 increases, the absolute value of $P_1 - P_2$ and changes in $P_1 - P_2$ are both much smaller than the value of P_1 anthe d corresponding changes in P_1 (Fig. 19). Thus, $P_1 - P_2$ can be approximated as a constant, Δ_p. Because the change in the uniform pressure loading P_1 - P_2 is much smaller than the corresponding change in P_1, and so the flow resistance before the channel does not contribute to pressure-compensating behavior (Eqn. 7).

The value of Δ_p depends on the geometry of the emitter. For the 2 L/hr emitter, for $P_1 > P_L$, Δ_p is 0.17 bar with a standard deviation of 0.037 bar. For the 1.1 L/hr emitter, Δ_p is 0.053 bar with a standard deviation of 0.016 bar. For the 3.8 L/hr emitter, Δ_p is 0.41 bar with a standard deviation of 0.071 bar. This relationship can be used to decrease the computational time of the hybrid model. For a given geometry, the number of iterations needed

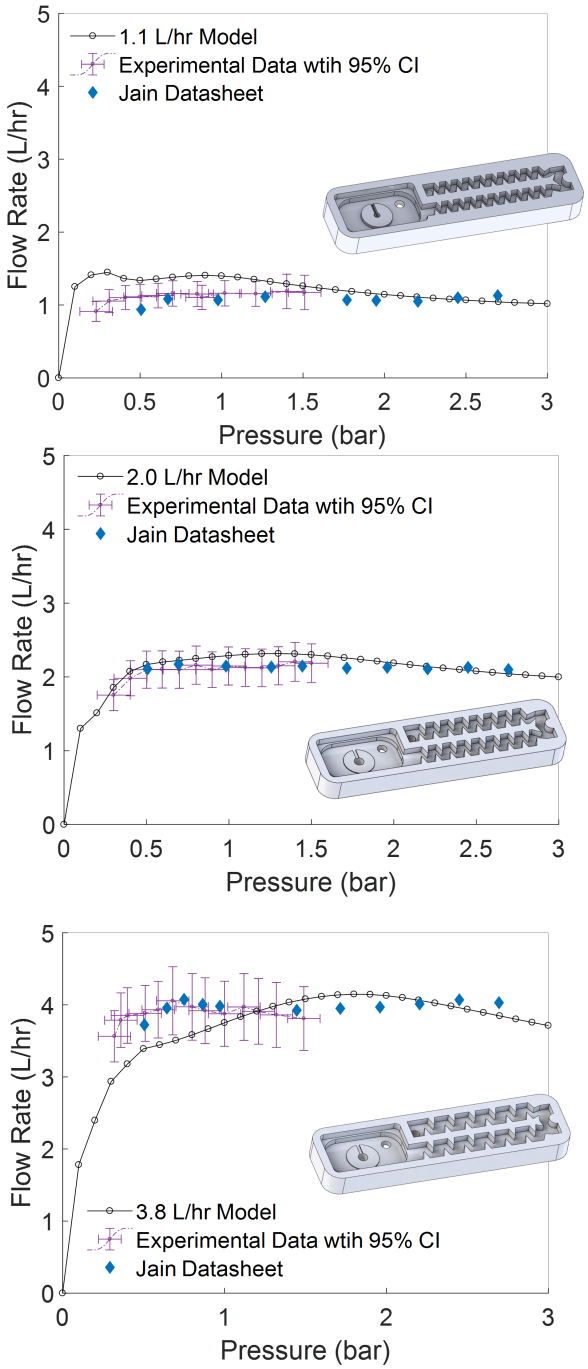

Figure 18. Flow rate behavior as a function of pressure as predicted by the hybrid computational-analytical model, and experimental data collected by the authors. The solid line shows the model predictions, with circles denoting individual data points. The purple dashed line shows experimental data, with crosses denoting individual data points. The blue diamonds are the published datasheet values [25]. The CAD model shown with each plot is of the corresponding emitter.

Table 2. Summary of calculated average flow rate and activation pressure for each emitter, using model predictions and experimental data over the range 0-1.5 bar

	1.1 L/hr Emitter	2.0 L/hr Emitter	3.8 L/hr Emitter
Avg. flow rate - model (L/hr)	1.38	2.09	3.47
P_{act} - model (bar)	0.1	0.3	0.35
Avg. flow rate - experiment (L/hr)	1.12	2.10	3.87
P_{act} - experiment (bar)	0.3	0.3	0.3

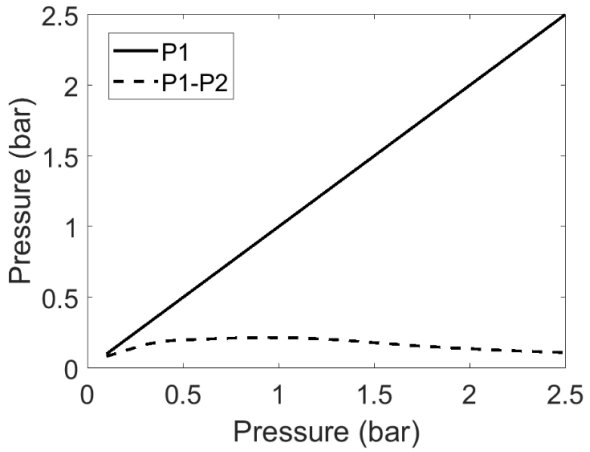

Figure 19. P_2 can be predicted by approximating $P_1 - P_2$ as a constant Δ_p because changes in $P_1 - P_2$ are much smaller than corresponding changes in P_1

for the model to converge can be reduced by first evaluating the hybrid model at an intermediate value of P_1, then estimating the constant Δ_p, and finally using the relationship $P_2 = P_1 + \Delta_p$ to guess an initial value of P_2 for each design point. Δ_p is a seed value used to increase convergence speed; it does not constrain the predicted value of P_2 and can be used when modeling emitters that do not have perfect PC behavior.

The hybrid computational-analytical model captured the pressure compensating behavior and flow rate for three distinct

emitter geometries. The model has a much wider range of applicability than published analytical models, in that it accounts for flow behavior through tortuous paths, and asymmetrical flow channels. The hybrid model has improved accuracy when compared to a purely analytical model [9].

The model makes some simplifications that likely contribute to the small inaccuracies apparent in Fig. 18. In the analytical model, the contact force between the membrane and the lands is approximated as a series of concentrated loads; however, the contact is actually a continuous distributed load applied over an increasing area. In the finite element model, the mesh is composed of two dimensional shell elements and assumes that the midplane deflection of the membrane is equal to the deflection of the bottom surface of the membrane. The analytical expressions for the flow assume locally fully developed flow, though a self-consistency check suggested that the flow may deviate from this behavior. The analysis of locally developed flow suggested that the flow models would have higher error at lower pressures, which is consistent with the results shown in Fig. 18.

The computational time required to fully model an emitter makes model-based design optimization extremely time and resource intensive. Generating the high-resolution CFD model predictions for a given path geometry such as those presented in Fig. 6 took four to six hours using five 2.4 GHz Intel Xeon Processor cores in parallel, depending on the geometry of the path. Modeling the contact between the membrane and the lands and coupling the fluid-structure interactions in a computational model would significantly more increase this time. Using the same processor, the hybrid computational-analytical model with simplifying assumptions presented herein can generate predictions of the similar resolution in approximately 30 minutes. This efficiency enables a level of iteration and optimization of emitter designs that would not be possible using other modeling approaches.

8 Conclusions

CFD and FEA are powerful but computationally intensive methods of modeling the behavior of inline drip emitters. Their long processing time makes it difficult to optimize the designs of drip emitters with tortuous paths and complex geometries.

Using a hybrid computational-analytical model significantly reduces the computational time required to model and optimize the behavior of PC inline drip emitters while maintaining a high level of accuracy. The model and techniques presented in this paper can be used to model a wide range of geometries. In the future, this method could be used to improve the design of inline drip emitters to lower activation pressure and material costs associated with manufacturing the emitter. Lowering the activation pressure could significantly reduce the energy costs associated with operating a drip irrigation system using the emitters.

Future work on this topic should include a range of design optimizations, and a broad model to analytically predict the flow behavior through a variety of path geometries.

ACKNOWLEDGMENT

The authors would like to acknowledge Jain Irrigation, Ltd., the National Science Foundation Graduate Research Fellowship Program, and the Tata Center for Technology and Design and for their support of this project. The authors would like to thank Abhijit Joshi and Sachin Patel of Jain Irrigation for their advice and expertise on drip irrigation, Andrea Meister for help with data collection, Susan Amrose and Julia Sokol for assistance reviewing the manuscript, and Pulkit Shamshery for background information on emitter modeling.

REFERENCES

[1] United Nations Enviornment Programme, 1998. Sourcebook of alternative technologies for freshwater augmentation in some countries in Asia. Tech. rep.

[2] Phansalkhar, S., and Verma, S., 2008. *Silver Bullets for the Poor: Off the Business Park*. IWMI-Tata Water Policy Program.

[3] Shamshery, P., and Amos G. Winter, V., 2017. "Shape and form optimization of online pressure compensating drip emitters to achieve lower activation pressure". *Journal of Mechanical Design*.

[4] Private, 2016. Private correspondance with jain irrigation inc. Jalgao, India.

[5] Glaad, Y., 1974. "Hydraulic and mechanical properties of drippers". In Proceedings of the Second International Drip Irrigation Conference.

[6] Palau-Salvador, G., Aryiza-Valverde, J., and Bralts, V., 1974. "Hydraulic flow behavior through an in-line emitter labyrinth using cfd techniques". In ASAE.

[7] Dazhuang, Y., Peiling, Y., Shumei, R., Yunkai, L., and Tingwu, X., 2007. "Numerical study on flow property in dentate path of drip emitters". *New Zealand Journal of Agricultural Research*, pp. 705–712.

[8] Wei, Q., Shi, Y., Dong, W., Lu, G., and Huang, S. "Study on hydraulic performance of drip emitter by computational fluid dynamics". *Agricultural Water Management,* **84**, pp. 130–136.

[9] Shamshery, P., Wang, R., Tran, D., and V, A. W., 2017. "Modeling the future of irrigation: a parametric description of pressure compensating drip irrigation emitter performance". *PlosOne*.

[10] Zhengying, W., 2013. "The step-by-step cfd design method of pressure-compensating emitter". *Engineering Sciences,* **11**, pp. 62–67.

[11] Wang, W., Bralts, V., and Wang, J., 2012. "A hydraulic analysis of an online pressure compensating emitter using cfd-csd technology". In ASAE Annual International Meeting.

[12] , 2018. Ansys modeling guide: The k-omega and sst models.

[13] Jain Irrigation Systems Ltd, 2016. Jain turbo excel. Web.

[14] Dai, Z., Fletcher, D. F., and Haynes, B. S., 2015. "Influence of tortuous geometry on the hydrodynamic characteristics of laminar flow in microchannels". *Chemical Engineering and Technology,* **38**, pp. 1406–1415.

[15] Yongxin, L., Guangyong, L., Xiangyu, Q., Jiandong, W., and Alam, M., 2005. "Computational fluid dynamics analysis and verification of hydraulic performance in drip irrigation emitters". In Irrigation Association International Irrigation Technical Conference.

[16] Gent, A. N., 2012. *Engineering with rubber: how to design rubber components*, 3rd ed. Hanser Publications.

[17] Ventsel, E., and Krauthammer, T., 2001. *Thin Plates and Shells: Theory, Analysis, and Applications*. Marcel Dekker Inc, New York, ch. Rectangular Plates, pp. 55–104.

[18] ASTM International, 2016. Designation d412-15a: Standard test methods for vulcanized rubber and thermoplastic elastomers - tension. Web.

[19] Young, W., and Budynas, R. G., 2002. *Roark's Formulas for Stress and Strain*. McGraw-Hill, ch. Beams: Flexure of Straight Bars, pp. 125–188.

[20] Ghugal, Y. M., and Sharma, R., 2011. "A refined shear deformation theory for flexure of thick beams". *Latin American Journal of Solids and Structures*, pp. 183–195.

[21] White, F., 1998. *Fluid Mechanics*. McGraw-Hill, ch. Viscous Flow in Ducts, pp. 325–405.

[22] McGovern, J., 2011. Technical note: Friction factor diagrams for pipe flow. Tech. rep., Dublin Institute of Technology, *.

[23] Pipeflow fluid thinking software solutions, 2012. Pipe roughness. Web.

[24] Sonin, A. A., 2002. "Criteria for locally fully developed viscous flow". *MIT Fluid Mechanics Course Materials*.

[25] Jain Irrigation Systems Ltd, 2016. Jain turbo cascade pc, pcnl, and pcas. Web.